

Article

The Effect of Calcination Temperature on the Structure and Performance of Nanocrystalline Mayenite Powders

Katarzyna Berent ^{1,*} , Sebastian Komarek ², Radosław Lach ² and Waldemar Pyda ²

¹ Academic Centre for Materials and Nanotechnology, AGH University of Science and Technology, 30 Mickiewicza Av., 30-059 Kraków, Poland

² Faculty of Materials Science and Ceramics, AGH University of Science and Technology, 30 Mickiewicza Av., 30-059 Kraków, Poland; seko@agh.edu.pl (S.K.); rlach@agh.edu.pl (R.L.); pyda@agh.edu.pl (W.P.)

* Correspondence: kberent@agh.edu.pl

Received: 23 August 2019; Accepted: 19 October 2019; Published: 24 October 2019



Abstract: The effect of calcination temperature on the structural properties and phase formation of synthesized CaO-Al₂O₃ nanopowder was investigated and discussed. The calcination products were identified by differential thermal analysis (DTA) and the crystalline phase formation was analyzed by X-ray diffraction (XRD). The obtained results showed that the crystallization started at 460 °C. Finally, the microstructures of the nanoparticles were observed by scanning (SEM) and transmission electron (TEM) microscopes. The investigation showed that an increase in the calcination temperature led to the appreciable increase in the crystallite size and the crystallinity of the final product. The obtained data confirmed that the prepared materials were mayenite with different surface area in the range of 71.18 m²/g to 10.34 m²/g after annealing in the temperature range of 470 °C to 960 °C.

Keywords: calcination temperature; calcium aluminate; mayenite; thermal behavior; nanocrystalline powder; microstructure

1. Introduction

The calcium aluminates, CaO-Al₂O₃ (C-A) system is a promising group of materials due to superior refractory properties. Especially, mayenite (12CaO·7Al₂O₃ labelled as C12A7) is an auspicious functional material for usage in various engineering applications, such as catalysis [1–4], in particular, used in the synthesis of ammonia [5,6], batteries [7], white light-emitting diodes (W-LEDs) [8], electronic [9] and optoelectronic devices [10], which results from the discovery of oxygen mobility [11] and ionic conductivity [12–14]. The unique properties of C12A7 come from its special crystal structure. The unit cell contains two formula units (Z = 2) and is convenient to define as [Ca₂₄Al₂₈O₆₄]⁴⁺ + 2O²⁻ [14]. It is composed of a Ca-Al-O framework forming interconnected 12 cages with a positive electric charge, the extra-framework highly mobile two oxygen ions occupy statistically two of these cages and compensate the charge of the framework [15,16]. On the one hand, the substitution for the free oxygen ions O²⁻ by F⁻, Cl⁻ and OH⁻ induces C12A7 into an electroneutral material in which electrons behave as anions [14].

The engineering applications of C-A powders depend considerably on their crystallite size and composition which are determined by the rate and temperature of calcination during synthesis [17]. Various preparation techniques, such as solid state routes [18], sol-gel [19–21], hydrothermal followed by calcination [17,22], the Pechini process [23], oxalate-precursor co-precipitation [24], the glycine/nitrate procedure-GNP [23,25], the spray pyrolysis method [26] and synthesis based on polymethyl methacrylate (PMMA) as a soft templating agent [27] are employed to prepare calcium aluminate powders composed of nanoparticles (NPs).

There is a growing interest in the synthesis of NPs in recent years, that possess unique physical and chemical properties due to their extremely high surface area and associated nanoscale size, which opens new possibilities for their applications. At these reduced dimensions, NPs provide a tremendous driving force for sintering, shorter distances for mass transportation and hence the surface energy of the nanoparticles substantially affects the interior bulk properties of the resultant materials [28]. In the case of NPs, the sintering can take place at lower temperatures, over shorter time scales, when compared to larger particles. Since the physical properties of ceramics are very sensitive to material density and microstructure, understanding the control of the above properties of the ceramics with respect to the ceramic processing parameters affected by sintering, such as a powder morphology, particles size, density and the sintering temperature is essential. Depending on the future application of C-A, the final morphology of the powder can be controlled. The sintering rate determines the growth rate of nanoparticles and is crucial for the design of their synthesis with controlled size, structure, composition. It is therefore, the objective of this study to investigate the effects of modification of calcination conditions on calcium aluminate phase transition, powder purity, mean size and morphology.

In the present work, we have employed a novel variant of the conventional method to synthesize nanocrystalline powders which combine the use of nanometric boehmite particles and submicron calcium hydroxide. The main advantage of this synthesis over the conventional ceramic process of the solid state reaction process is the decreased temperature of reaction and nanometric size of the powder. The microstructure of the synthesized powders can be modified by changing reaction conditions to achieve the desired final product. Several analytical techniques such as thermogravimetric (TG/DTA), X-ray diffraction (XRD), transmission and scanning electron microscopy (TEM, SEM) were used to understand the changes in the synthesized material during the thermal calcination process.

2. Materials and Methods

The new combinational method of production of CaO-Al₂O₃ nanopowders under study comprised several steps. In the first one, a boehmite gel (γ -AlO(OH)) was obtained using nanocrystalline (20 nm) dawsonite (NH₄AlCO₃(OH)₂), synthesized from aqueous saturated solutions of aluminium nitrate enneahydrate (Al(NO₃)₃·9H₂O) (p.a.) and ammonium carbonate ((NH₄)₂CO₃) (p.a.), which was subjected to a hydrothermal treatment in a stainless-steel autoclave for 2 h at 130 °C at 100 kPa pressure. Then, the formed nanocrystalline γ -AlO(OH) (crystallite size 3.7 nm), being in the form of a gel-like aqueous colloidal suspension, was mixed with Ca(OH)₂ (p.a.) particles in a molar ratio of 14:12. The reactants were homogenized using a mixer mill at RT, dried in a laboratory dryer at 100 °C for constant weight and again ground for 15 min in a corundum mortar. Finally, the obtained powder was calcined in a conventional electric furnace for 30 min at different temperatures of 170 °C, 470 °C, 760 °C, 960 °C and 1250 °C under air atmosphere.

The thermogravimetric (TG/DTA) curves were recorded on a simultaneous thermal analyzer (STA 449 F3, NETZSCH, Selb, Germany). The instrument was operated from ambient to 1400 °C at a heating rate of 10 °C/min in atmospheric air.

The phase identification was performed by X-ray diffraction using an X-ray diffractometer (Empyrean, Malvern Panalytical, Malvern, UK) with Cu K α radiation ($\lambda = 1.5406 \text{ \AA}$). Data were collected in the 2θ range of 10–89.90° with a resolution of 0.008°. The crystallite size of the calcined powders was determined by the X-ray line broadening technique performed on the most intense diffraction peak from the (420) plane of mayenite using the Scherrer equation [29]:

$$D = \frac{0.9\lambda}{\sqrt{\beta_{\text{sample}}^2 - \beta_{\text{ref}}^2} \cos\theta} \quad (1)$$

where D is the crystallite size (nm), λ is the wavelength of CuK α radiation, which equals to 0.154 nm, β_{sample} is the FWHM of a diffraction peak and β_{ref} corresponds to the instrumental FWHM and θ is the Bragg angle.

The morphological structure was studied using a scanning electron microscope (Versa 3D, FEI Company, Hillsboro, OR, USA) whereas the exact dimensions of the nanopowders were investigated using transmission electron microscopy (Tecnai 200, FEI Company, Hillsboro, OR, USA). The samples for SEM and TEM were prepared by dispersing the calcined powder particles in alcohol and then dropped onto a carbon film supported on a copper grid. The TEM image analysis was done by measuring two perpendicular diameters from the particle with ImageJ software and then the diameter was calculated as the average dimension along the two axes.

The Brunauer–Emmer–Teller (BET) surface area was determined by means of the adsorption/desorption isotherms of liquid nitrogen at $-196\text{ }^{\circ}\text{C}$ using an automatic analyzer (ASAP 2000, Micromeritics Inc. Corp., Norcross, GA, USA).

3. Results and Discussion

3.1. Thermal Behaviour of the Precursor Mixture

The TG/DTA technique was very useful in the characterization of the thermal behavior of the mayenite precursor mixture. Figure 1a shows the thermal evolution of the temperature range of RT to $1400\text{ }^{\circ}\text{C}$. Mass spectrometry (MS) results that present ion currents of NH_3 , H_2O , CO_2 and NO in gases released from samples during the TG/DTA experiment are additionally shown in Figure 1b.

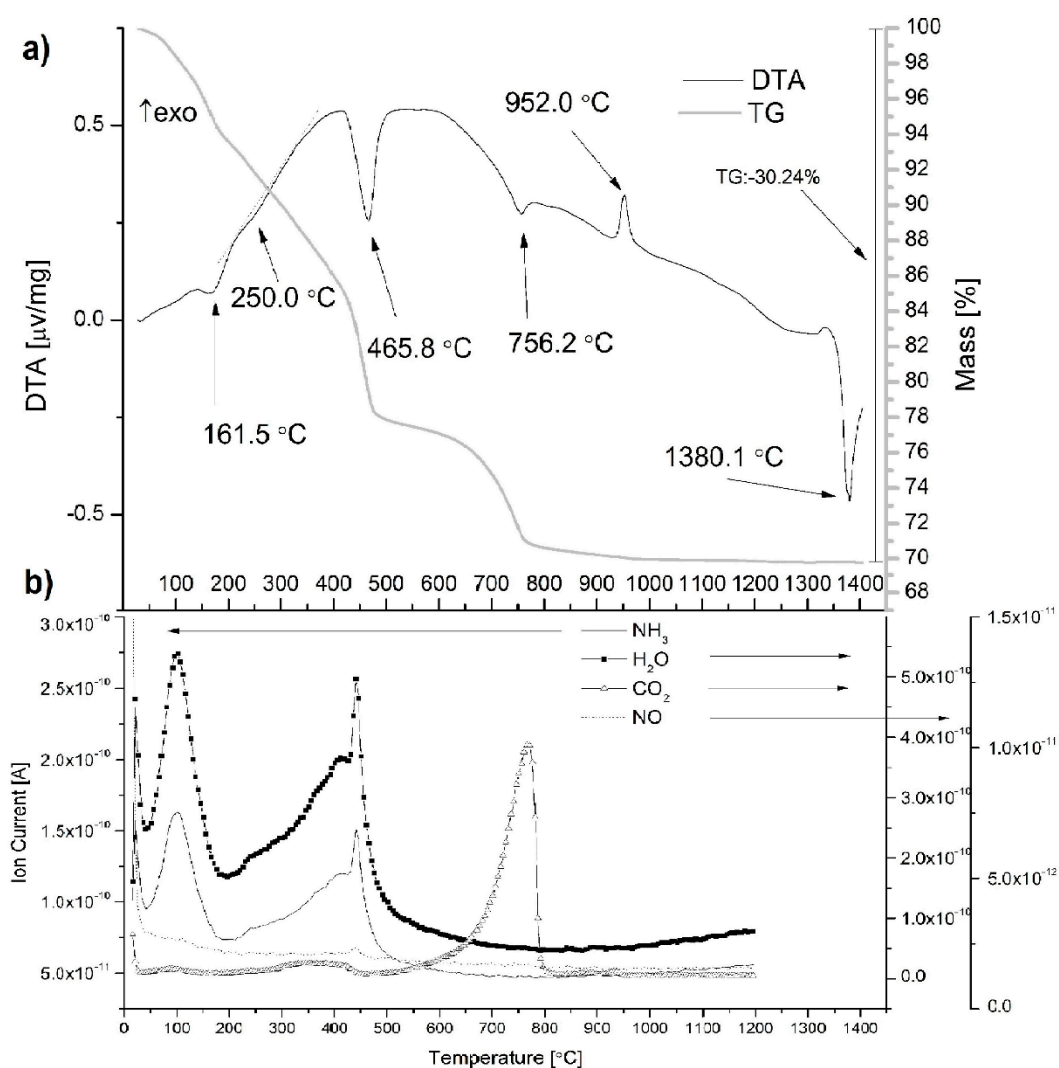


Figure 1. TG/DTA curves (a), and selected curves of mass-spectroscopic ion currents (b) for gases evolved during heating from the as-synthesized powder.

A correct interpretation of the results of TG/DTA and released gases requires knowledge of the phase composition of the tested mixture of mayenite precursors, which is given in Figure 2. The main components of this mixture, which was dried to constant weight at 100 °C, were nano-boehmite and calcium hydroxide, but the hydrogranet phase ($\text{Ca}_3\text{Al}_2(\text{OH})_{12}$, C3AH6) in the amount of 23.3 wt %, which is already formed at 45 °C according to [30], was also found. Calcium carbonate was introduced into the mixture together with calcium hydroxide in which it was present in an amount of 3.99%, as revealed by TG/DTA analysis of this reagent. The probable presence of $\gamma\text{-Al}_2\text{O}_3$ would be associated with the dehydration of some nano-boehmite crystallites.

Essentially six endothermic peaks are observed: extremely weak at 100 °C, then pronounced at 161.5 °C, blurred at ~250 °C, intense at 465.8 °C and weaker at 756.2 °C; these effects are accompanied by correlated weight losses, as shown by the TG curve. The last endothermic peak occurs at 1380.1 °C, and the sample does not change its mass. The exothermic peak is observed only at 952 °C.

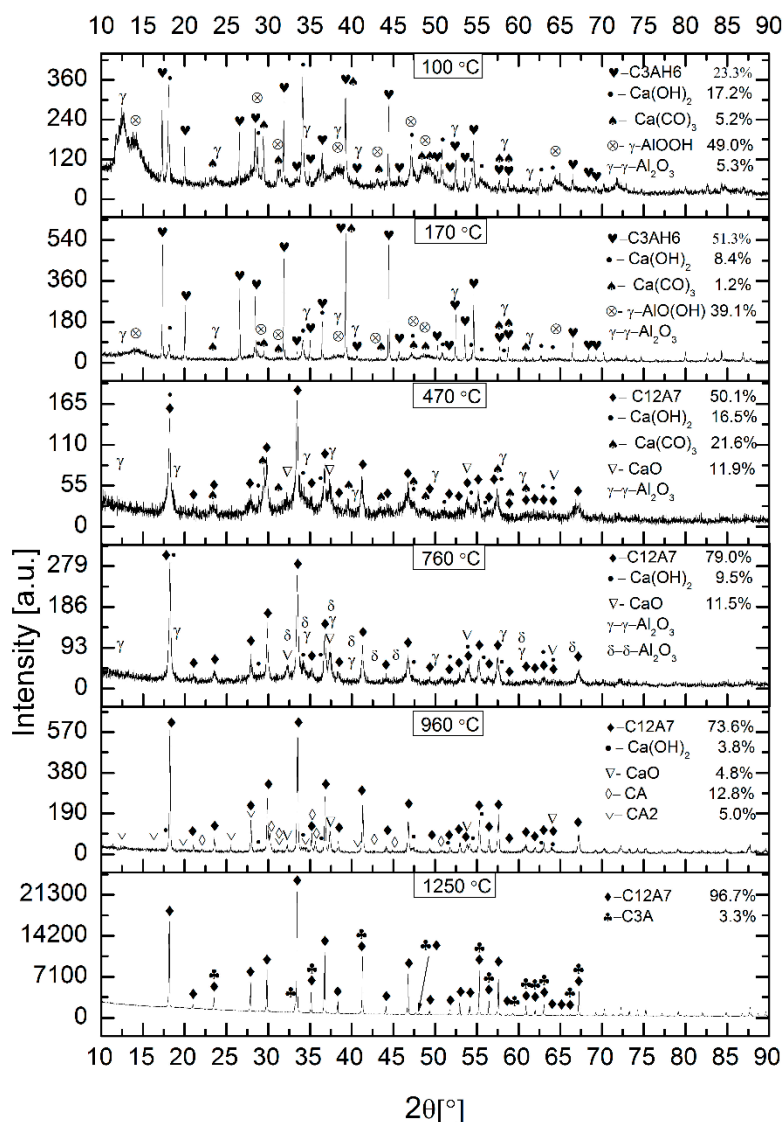
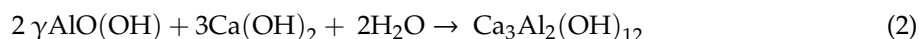


Figure 2. XRD patterns of powders calcined at different temperatures; phase names are indicated together with their weight contents.

Several components, such as the physically adsorbed species like water and organic molecules are removed from the system at the lower temperature range [31,32]. The maxima on the H₂O, NH₃ and CO₂ ion current curves at 100 °C (Figure 1b), which correspond to the extremely poorly marked

endothermic peak on the DTA curve (Figure 1a), should be attributed to the desorption of these molecules from the surface of the particles of the phases that formed the mixture of mayenite precursors.

The second endothermic peak appears at 161.5 °C, which is attributed to a small mass loss. The initial decrease in mass occurs after the beginning of the heating stage it is related to the beginning of the reaction of forming additional portions of C3AH6 from unreacted nano-boehmite and calcium hydroxide particles according to the following equation [6]:



The highest rate of hydrogarnet formation falls at 161.5 °C. Since this reaction consumes water molecules in the range from ~45 °C to ~200 °C, the ion current for water molecules is the combined effect of water desorption processes and hydrogarnet formation.

The third broad and weak endothermic peak appears at 250 °C, due to the dehydration of C3AH6, which leads to a transition into C12A7, which is the hydrated state described as $\text{Ca}_{12}\text{Al}_{14}\text{O}_{33} \cdot \text{H}_2\text{O}$ (C12A7H). Simultaneously $\text{Ca}(\text{OH})_2$ is formed and is further converted to CaO (and CaCO_3 in air) above ~350 °C [6]. The reaction of forming hydrated C12A7 is presented in the following equation:



The proposed reaction is in line with the increase in the ionic current of the released water molecules, which is observed in the hydrogarnet dehydration temperature range. In this range, NH_3 and CO_2 molecules are also released, proving their binding to the structure of formed mayenite crystallites.

The fourth endothermic peak emerging at about 465.8 °C is due to the dehydration of $\text{Ca}(\text{OH})_2$ to yield CaO according to the reaction [33]:



This endothermic event is accompanied by weight loss, as well as the release of H_2O , NH_3 and additionally NO molecules (Figure 1b). The temperature of this peak agrees well with a temperature of 468 °C determined in a separate TG/DTA measurement for the decomposition of calcium hydroxide. This study also revealed the presence of 3.99% calcium carbonate, which decomposed at 703 °C.

The fifth endothermic peak around 756.2 °C is assigned to the decomposition of CaCO_3 according to the reaction:



This peak is accompanied by weight loss and CO_2 release, as shown in Figure 2a,b, respectively. Primary CaCO_3 contained in the initial calcium hydroxide and secondary CaCO_3 derived from the decomposition of the hydrogarnet gave a contribution to the observed thermal effect.

It can be concluded that the formation of monocalcium aluminate (CaAl_2O_4 , CA) is observed at 952.0 °C, as revealed by the XRD patterns [20].



The sixth endothermic peak emerging at about 1380.1 °C is attributed to the melting of $\text{Ca}_{12}\text{Al}_{14}\text{O}_{33}$, which indicates that the phase transformation occurred.

3.2. Phase Analysis of the Product

The component phases of the product were examined with XRD, and qualitative agreement with literature data was obtained. Figure 2 shows the XRD patterns of the as-prepared mixture and those calcined at 100 °C, 170 °C, 470 °C, 760 °C, 960 °C and 1250 °C, respectively.

For the sample annealed at 170 °C, there are peaks corresponding to the form of C3AH6, $\text{Ca}(\text{OH})_2$, $\text{Ca}(\text{CO})_3$, $\gamma\text{-AlO}(\text{OH})$. Aluminium phase with a structure similar to $\gamma\text{-Al}_2\text{O}_3$ is probably present at

this temperature. However, the indexing is difficult due to the low intensity peaks. C3AH6 formation during heat treatment at 161.5 °C in accordance with reaction (1) is marked by the increase in the amount compared to the initial sample of the precursor mixture and the simultaneous increase in the content of boehmite and calcium hydroxide.

After calcination at 470 °C, complete disappearance of the hydrogarnet is observed along with the appearance of the mayenite phase, probably hydrated (C12A7H) together with CaO and some amounts of Ca(OH)₂, Ca(CO)₃, and γ -Al₂O₃. Lack of anhydrous hydrogarnet phase [17,32,34,35] in the sample heat treated at 170 °C and increased the content of calcium hydroxide, calcium carbonate and calcium oxide in the sample from 470 °C suggests the mechanism of mayenite formation. According to this mechanism (Equation (2)) the topotactic decomposition of hydrogarnet occurs at temperature exceeding ~220 °C, as indicated by TG/DTA measurements. The presence of significant amounts of calcium hydroxide indicates only its partial decomposition under used heat treatment conditions.

At higher temperatures, γ -Al₂O₃ decomposes into δ -Al₂O₃ [32], and the formation of CaO from the decomposition of calcium carbonate is observed. Thus, increasing the temperature of the heat treatment of the precursor mixture to 760 °C resulted in the complete decomposition of Ca(CO)₃, a significant reduction in the calcium hydroxide content with a slight change in the CaO content, but also a significant increase in the C12A7 content by ~30 wt %. The phases γ -Al₂O₃ and δ -Al₂O₃ occurred in an amount impossible to measure reliably. It should be noted, therefore, that failure to include aluminium phases in the phase composition of the 470 °C and 760 °C samples means that the calculations of the component phase contents are only indicative and allow only a qualitative interpretation of these results. There is no doubt that the increase in C12A7's content in the absence of a hydrogarnet as a precursor suggests a mechanism responsible for this fact other than topotactic degradation of the hydrogarnet. The results of X-ray studies indicate a direct reaction of oxide precursors of the C12A7 phase with the participation of solid state diffusion and the use of the process of nucleating new crystallites on the surfaces of already existing crystalline mayenite particles or growing atom by atom of these surfaces. Often the presence of CA may hasten the set time of the CA2 phase, which is why it appears in aluminous cements as a secondary phase [36].

Further, by increasing the calcination temperature to 960 °C, the XRD pattern indicates the formation of new aluminate phases: CA and monocalcium dialuminate (CaAl₄O₇, CA2) at the expense of a significant reduction in the content of calcium hydroxide and calcium oxide with virtually unchanged contribution of C12A7 (this result may be underestimated due to the fact that the unmeasured amount of aluminium oxide was not included in the calculations). This clear variation in the phase composition may have its source in the initial heterogeneity of the mixture of nano-boehmite and calcium hydroxide much coarser. This heterogeneity could even deepen during the formation of phase composition.

The highest heat treatment temperature used was 1250 °C had a very positive effect on the homogeneity of the phase composition. The content of C12A7 increased to 96.7 wt %, and as the second phase, tricalcium aluminate (3CaO·Al₂O₃, C3A) is present in the amount of 3.3 wt %, which is formed in the reaction between C12A7 and CaO [37].

The width of the diffraction peaks of the mayenite phase (Figure 2) and data of Table 1 confirm the nanocrystalline nature of the prepared materials. The crystallite size of primary particles is measured by the XRD method and they are higher as the calcination temperature increases. The thermodynamically justified phenomenon of crystallite size growth with increasing calcination temperature is associated with the enhancement of the ratio of crystalline volume to the surface, which occurs as a result of enlargement of the particle size, reducing the Gibbs free energy of the system [38].

As shown in Table 1, the average crystallite size D_{XRD} of mayenite particles increases with the increase of the calcination temperature from 31.1 nm to 81.3 nm in the studied temperature range. By comprehensive consideration, the optimal calcination temperature for the precursor mixture used is 470 °C, due to the appropriate crystallinity fraction and the smallest crystallite size.

Table 1. BET surface area and the average crystallite/particle size of CA powders.

Sample	S_{BET} (m ² /g)	Crystallite/Particles Size [nm]	
		D_{XRD}	D_{TEM}
470 °C	71.18 ± 0.20	31.1	10.7
760 °C	50.26 ± 0.08	44.9	17.6
960 °C	10.34 ± 0.04	81.3	78.1

3.3. Microstructural Characterizations

The morphologies of the four examined powders obtained at various temperatures are shown in the micrographs in Figure 3.

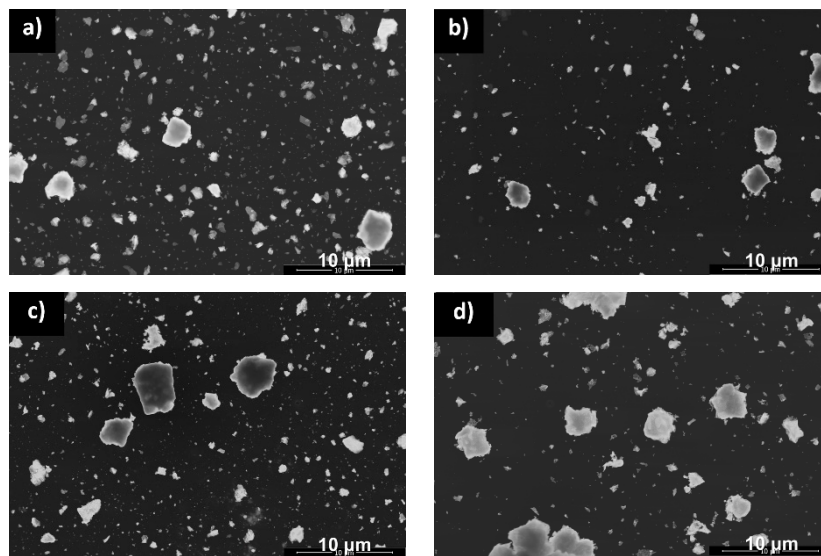


Figure 3. SEM micrographs of the powders calcined at different temperatures 170 °C (a), 470 °C (b), 760 °C (c) and 960 °C (d).

The formation of the aggregates from the primary particles is observed for all samples. A worm-like structure of primary particles can be noticed with large, irregularly shaped particles with 0.2–3.4 μm in diameter. Although the XRD analysis results indicate that the crystallite size increases with the increase of calcination temperature, this regulation cannot be directly recognized from the SEM images due to limitations of the method. TEM was used to improve the spatial resolution and the image quality of the primary crystallites.

The selected samples were subjected to TEM analysis for a better understanding of the effects of the calcination process on the morphology and phase formation of nanopowders. Figure 4 shows the bright field (BF) images and the corresponding selected area electron diffraction (SAED) patterns of the as-prepared powders calcined at 470 °C, 760 °C and 960 °C, respectively.

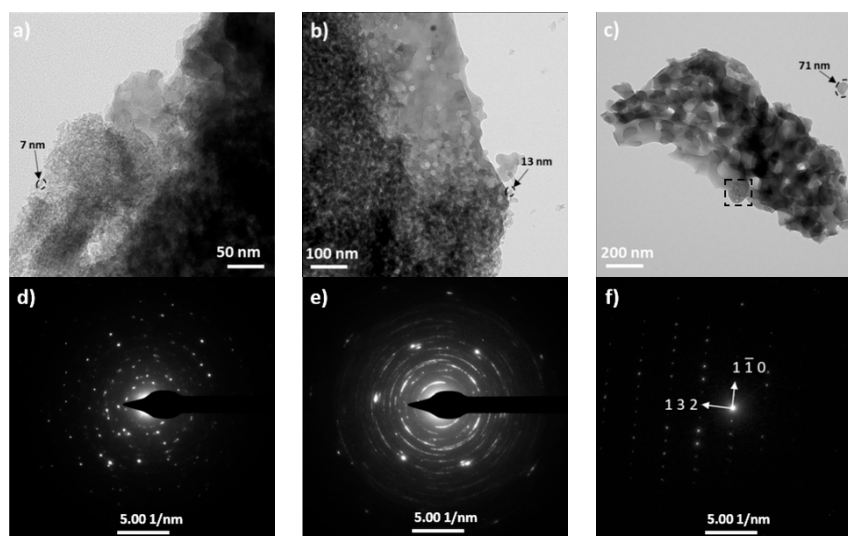


Figure 4. TEM micrographs and the corresponding SAED patterns of the powders calcined at 470 °C (a,d), 760 °C (b,e) and 960 °C (c,f).

It can be observed that the primary particle morphology is nearly spherical and of uniform size with clear aggregation. The BF image of the sample calcined at 470 °C (Figure 4a) shows that it contains nanoparticles having sizes of ~5–13 nm whereas the powder calcined at 760 °C (Figure 4b) consists of particles of ~10–25 nm in diameter. The primary particles obtained in the lower temperatures show a narrow size distribution. Sinter necks are not observed for the samples sintered at lower temperatures. When raising the calcination temperature for a fixed isothermal time, the grain size of the CA grew significantly. The nanoparticles calcined at 960 °C consisted of large grains such as spheroidal shape particles that the surfaces of several neighboring particles were melted during the procedure due to the high temperature value. Under this condition, the primary crystallites are bonded together by solid bridges (typically formed during the calcination process). The BF micrograph (Figure 4c) reveals the presence of nonuniform aggregates and an internal porosity. Different types of aggregation are marked by a black square in the BF images. The SAED patterns (Figure 4d–f) showing diffuse rings and regular spots which confirms the crystallinity of the powders and is in good agreement with the XRD patterns. The primary particles obtained at lower temperatures turn out a continuous ring pattern due to the presence of a large number of single crystallites in the selected area. However, when the primary particle size increases at higher calcination temperature, the spots are far from each other. The crystal structure analysis using SAED fitted to the cubic crystal structure of mayenite with the $I-43d$ space group and lattice parameters $a = 11.982$ nm (Figure 4c). It has a narrow particle size distribution ranging between 10.7 and 78.1 nm. The average TEM particle size of the nanocrystallites is shown in Table 1. The observed (sub)micrometric particles by SEM are porous agglomerates of nanometric primary crystallites as confirmed by the TEM studies. At an increasing calcination temperature, a continuous agglomeration of primary particles ensued and when the agglomeration is concluded, the rapid growth of isolated and connected particle was observed. Therefore, at the highest calcination temperature, the pores in the materials are trapped as a result of the sintering.

The relation between the BET surface area (S_{BET}) and the calcination temperature of the powders is shown in Table 1. It can be noticed that the powder calcined at 470 °C has the highest BET surface area equal to 71.18 m²/g. The values gradually decrease with increasing calcination temperature and for heating the powder at 960 °C has 10.34 m²/g. The observed decrease in the S_{BET} can be attributed to the increase in the crystallite size as confirmed by the XRD and TEM results. The obtained results are in accordance with the works of other authors. Li et al. report that the specific surface area of the mayenite prepared by the hydrothermal method and calcined at 400 °C for 4 h amounted to about 67.1 m²/g [22]. A novel route based on the use of polymethyl methacrylate (PMMA) described by Intiso et al. [27]

allows to obtain the mayenite powder with the largest surface area of 47.1 m²/g for mayenite prepared using 10% w/w of PMMA. The crystallite size (D_{XRD}) and the particle size (D_{TEM}) data show some discrepancies, indicating that the primary crystallites are significantly agglomerated. The results show that the crystallite growth may be divided into three different ranges between 470 °C and 960 °C. In the temperature of 470 °C, where the nanoporous structure still remains intact, the crystallite growth was slow and the BET surface area remained the highest value. Then, at a temperature of 760 °C, an increase of the primary crystallite size and degree of agglomeration is observed. Finally, the melting of the particles and sintering occurred at a temperature of 960 °C. That is the reason why the crystallite size D_{XRD} shows larger values than that expected from the TEM analysis, which might be associated with a highly agglomerated structure observed in the TEM micrographs [39]. The differences in the primary particles sizes can be envisaged taking into account that the TEM images show the real powder particles size while XRD measurements are sensitive to the extension of optically coherent areas.

4. Conclusions

In this study, the effect of calcination temperature on the phase and microstructure evolution was investigated and the following summary can be made based on the results:

1. Proposed synthesis process effectively enhanced the reactivity of the substrates due to their nanometric size of boehmite. The nanocrystalline mayenite powders can be easily obtained using this method at temperatures of 470 °C a result of dehydration of the C3AH6 hydrogranate above 220 °C. Further portions of C12A17 are formed by the solid state reaction of the constituent oxides at higher temperatures;
2. It was found that calcination temperature is an important factor in the synthesis of nanocrystalline C12A7 powders, and the formation of aluminate phases depends on it. In the case of powders synthesized at lower temperatures, the presence of small amounts of Ca(OH)₂ and CaO are observed which indicates only its partial decomposition under the heat treatment conditions. Reducing the proportion of these compounds after thermal reduction can occur through the washing of the precursors by 0.1 M NH₄Cl/methanol solution mixture, which allows for their chemoselective dissolution [6];
3. Powders with a high BET surface area of around 71.18 m²/g containing C12A14H as the main phase showing 10.7 nm crystallite size can be synthesized followed by a relatively low temperature calcination of around 470 °C compared to the routine ceramic method involving solid state reaction, which requires over 1000 °C to form the same phase, but a very low BET surface area of below 10 m²/g [22]. Use of a novel synthetic route based on the use of PMMA as a soft templating agent [27] also does not give the possibility of synthesizing mayenite powders with such a large surface area as the hydrothermal method allows.

Author Contributions: Conceptualization, K.B. and W.P.; formal analysis, K.B. and S.K.; investigation, K.B., S.K. and R.L.; methodology, K.B. and W.P.; writing—original draft, K.B.; writing—review and editing, S.K., R.L. and W.P.

Funding: This research was funded by the National Science Centre in Poland, grant number 2014/15/D/ST8/02630 SONATA 8.

Acknowledgments: The authors thank Marta Gajewska from the AGH University of Science and Technology, Academic Centre for Materials and Nanotechnology for the TEM measurements.

Conflicts of Interest: The authors declare no conflict of interest. The funders had no role in the design of the study; in the collection, analyses, or interpretation of data; in the writing of the manuscript, or in the decision to publish the results.

References

1. Proto, A.; Cucciniello, R.; Genga, A.; Capacchione, C. A study on the catalytic hydrogenation of aldehydes using mayenite as active support for palladium. *Catal. Commun.* **2015**, *68*, 41–45. [[CrossRef](#)]

2. Suzuki, K. Application to catalyst of mayenite consisting of ubiquitous elements. *Trans. JWRI* **2010**, *39*, 281–283.
3. Cucciniello, R.; Intiso, A.; Castiglione, S.; Genga, A.; Proto, A.; Rossi, F. Total oxidation of trichloroethylene over mayenite ($\text{Ca}_{12}\text{Al}_{14}\text{O}_{33}$) catalyst. *Appl. Catal. B Environ.* **2017**, *204*, 167–172. [[CrossRef](#)]
4. Ruszak, M.; Inger, M.; Witkowski, S.; Wilk, M.; Kotarba, A.; Sojka, Z. Selective N_2O Removal from the Process Gas of Nitric Acid Plants Over Ceramic $12\text{CaO} \cdot 7\text{Al}_2\text{O}_3$ Catalyst. *Catal. Lett.* **2008**, *126*, 72–77. [[CrossRef](#)]
5. Kitano, M.; Inoue, Y.; Yamazaki, Y.; Hayashi, F.; Kanbara, S.; Matsuishi, S.; Yokoyama, T.; Kim, S.W.; Hara, M.; Hosono, H. Ammonia synthesis using a stable electride as an electron donor and reversible hydrogen store. *Nat. Chem.* **2012**, *4*, 934–940. [[CrossRef](#)] [[PubMed](#)]
6. Hasegawa, G.; Moriya, S.; Inada, M.; Kitano, M.; Okunaka, M.; Yamamoto, T.; Matsukawa, Y.; Nishimi, K.; Shima, K.; Enomoto, N.; et al. Topotactic Synthesis of Mesoporous $12\text{CaO} \cdot 7\text{Al}_2\text{O}_3$ Mesocrystalline Microcubes toward Catalytic Ammonia Synthesis. *Chem. Mater.* **2018**, *30*, 4498–4502. [[CrossRef](#)]
7. Chen, G.; Bai, Y.; Li, H.; Li, Y.; Wang, Z.; Ni, Q.; Liu, L.; Wu, F.; Yao, Y.; Wu, C. Multilayered electride Ca_2N electrode via compression molding fabrication for sodium ion batteries. *ACS Appl. Mater. Interfaces* **2017**, *9*, 6666–6669. [[CrossRef](#)]
8. Liu, X.L.; Liu, Y.X.; Yan, D.T.; Zhu, H.C.; Liu, C.G.; Xu, C.S. Luminescence and energy transfer characteristics of Ce^{3+} - and Tb^{3+} -codoped nanoporous $12\text{CaO} \cdot 7\text{Al}_2\text{O}_3$ phosphors. *J. Nanosci. Nanotechnol.* **2011**, *11*, 9953–9957. [[CrossRef](#)]
9. Johnson, L.E.; Sushko, P.V.; Tomota, Y.; Hosono, H. Electron anions and the glass transition temperature. *Proc. Natl. Acad. Sci. USA* **2016**, *113*, 10007–10012. [[CrossRef](#)]
10. Hosono, H.; Kim, J.; Toda, Y.; Kamiya, T.; Watanabe, S. Transparent amorphous oxide semiconductors for organic electronics: Application to inverted OLEDs. *Proc. Natl. Acad. Sci. USA* **2017**, *114*, 233–238. [[CrossRef](#)]
11. Teusner, M.; De Souza, R.A.; Krause, H.; Ebbinghaus, S.G.; Belghoul, B.; Martin, M. Oxygen Diffusion in Mayenite. *J. Phys. Chem. C* **2015**, *119*, 9721–9727. [[CrossRef](#)]
12. Matsuishi, S.; Toda, Y.; Miyakawa, M.; Hayashi, K.; Kamiya, T.; Hirano, M.; Tanaka, I.; Hosono, H. High-Density Electron Anions in a Nanoporous Single Crystal: $[\text{Ca}_{24}\text{Al}_{28}\text{O}_{64}]^{4+}(4e^-)$. *Science* **2003**, *301*, 626–629. [[CrossRef](#)] [[PubMed](#)]
13. Strandbakke, R.; Kongshaug, C.; Haugsrud, R.; Norby, T. High-Temperature Hydration and Conductivity of Mayenite, $\text{Ca}_{12}\text{Al}_{14}\text{O}_{33}$. *J. Phys. Chem. C* **2009**, *113*, 8938–8944. [[CrossRef](#)]
14. Hayashi, K.; Hirano, M.; Hosono, H. Functionalities of a Nanoporous Crystal $12\text{CaO} \cdot 7\text{Al}_2\text{O}_3$ Originating from the Incorporation of Active Anions. *Bull. Chem. Soc. Jpn.* **2007**, *80*, 872–884. [[CrossRef](#)]
15. Huang, J.; Valenzano, L.; Sant, G. Framework and Channel Modifications in Mayenite ($12\text{CaO} \cdot 7\text{Al}_2\text{O}_3$) Nanocages by Cationic Doping. *Chem. Mater.* **2015**, *27*, 4731–4741. [[CrossRef](#)]
16. Boysen, H.; Kaiser-Bischoff, I.; Lerch, M. Anion diffusion processes in O- and N-mayenite investigated by neutron powder diffraction. *Diffus. Fundam.* **2008**, *8*, 1–2.
17. Khan, K.; Li, J.; Zou, W.; Xu, W.; Yang, Y.; Song, W. Low temperature synthesis of nano porous $12\text{CaO} \cdot 7\text{Al}_2\text{O}_3$ powder by hydrothermal method. *J. Wuhan Univ. Technol. Sci. Ed.* **2016**, *31*, 1201–1205. [[CrossRef](#)]
18. Boysen, H.; Lerch, M.; Stys, A.; Senyshyn, A. Structure and oxygen mobility in mayenite ($\text{Ca}_{12}\text{Al}_{14}\text{O}_{33}$): A high-temperature neutron powder diffraction study. *Acta Crystallogr. Sect. B Struct. Sci.* **2007**, *63*, 675–682. [[CrossRef](#)]
19. Gong, L.; Lin, Z.; Ning, S.; Sun, J.; Shen, J.; Torimoto, Y.; Li, Q. Synthesis and characteristics of the $\text{C}_{12}\text{A}_7\text{-O}^-$ nanoparticles by citric acid sol-gel combustion method. *Mater. Lett.* **2010**, *64*, 1322–1324. [[CrossRef](#)]
20. Ude, S.N.; Rawn, C.J.; Peascoe, R.A.; Kirkham, M.J.; Jones, G.L.; Payzant, E.A. High temperature X-ray studies of mayenite synthesized using the citrate sol-gel method. *Ceram. Int.* **2014**, *40*, 1117–1123. [[CrossRef](#)]
21. Salasin, J.R.; Rawn, C. In-Situ Kinetic Investigation of Calcium Aluminate Formation. *Ceramics* **2018**, *1*, 175–197. [[CrossRef](#)]
22. Li, C.; Hirabayashi, D.; Suzuki, K. Synthesis of higher surface area mayenite by hydrothermal method. *Mater. Res. Bull.* **2011**, *46*, 1307–1310. [[CrossRef](#)]
23. Raab, B.; Poellmann, H. Heat flow calorimetry and SEM investigations to characterize the hydration at different temperatures of different $12\text{CaO} \cdot \text{Al}_2\text{O}_3$ (C_{12}A_7) samples synthesized by solid state reaction, polymer precursor process and glycine nitrate process. *Thermochim. Acta* **2011**, *513*, 106–111. [[CrossRef](#)]

24. Rashad, M.M.; Mostafa, A.G.; Rayan, D.A. Structural and optical properties of nanocrystalline mayenite $\text{Ca}_{12}\text{Al}_{14}\text{O}_{33}$ powders synthesized using a novel route. *J. Mater. Sci. Mater. Electron.* **2016**, *27*, 2614–2623. [[CrossRef](#)]
25. Matović, B.; Prekajski, M.; Pantić, J.; Bräuniger, T.; Rosić, M.; Zagorac, D.; Milivojević, D. Synthesis and densification of single-phase mayenite (C_{12}A_7). *J. Eur. Ceram. Soc.* **2016**, *36*, 4237–4241. [[CrossRef](#)]
26. Kerrou, W.; Kabir, A.; Schmerber, G.; Boudjema, B.; Zerkout, S.; Bouabellou, A.; Sedrati, C. Characterization of C_{12}A_7 thin films deposited by spray pyrolysis. *J. Mater. Sci. Mater. Electron.* **2016**, *27*, 10106–10112. [[CrossRef](#)]
27. Intiso, A.; Martinez-Triguero, J.; Cucciniello, R.; Proto, A.; Palomares, A.E.; Rossi, F. A Novel Synthetic Route to Prepare High Surface Area Mayenite Catalyst for TCE Oxidation. *Catalysts* **2019**, *9*, 27. [[CrossRef](#)]
28. Thatikonda, S.K.; Goswami, D.; Dobbidi, P. Effects of CeO_2 nanoparticles and annealing temperature on the microwave dielectric properties of MgTiO_3 ceramics. *Ceram. Int.* **2014**, *40*, 1125–1131. [[CrossRef](#)]
29. Azaroff, L.V. *Element of X-ray Crystallography*; McGraw-Hill: New York, NY, USA, 1968.
30. Kurdowski, W. *Chemia Cementu i Betonu*; Wydawnictwo Naukowe PWN: Warsaw, Poland, 1990.
31. Prabhakaran, K.; Ananthakumar, S.; Pavithran, C. Gel Casting of Alumina using Boehmite as a Binder. *J. Eur. Ceram. Soc.* **1999**, *19*, 2875–2881. [[CrossRef](#)]
32. Pyda, W.; Kędzierska, A.; Morgiel, J.; Moskała, N. Calcined aluminium oxide nanopowders of boehmite origin and narrow particle size distribution. *Mater. Ceram.* **2016**, *68*, 376–383.
33. Hayashi, K.; Hirano, M.; Hosono, H. Thermodynamics and Kinetics of Hydroxide Ion Formation in $12\text{CaO}\cdot 7\text{Al}_2\text{O}_3$. *J. Phys. Chem. B* **2005**, *109*, 11900–11906. [[CrossRef](#)] [[PubMed](#)]
34. Rivas-Mercury, J.M.; Pena, P.; de Aza, A.H.; Turrillasc, X. Dehydration of $\text{Ca}_3\text{Al}_2(\text{SiO}_4)_y(\text{OH})_{4(3-y)}$ ($0 < y < 0.176$) studied by neutron thermodiffractometry. *J. Eur. Ceram. Soc.* **2008**, *28*, 1737–1748. [[CrossRef](#)]
35. Hayashi, K.; Ueda, N.; Matsuishi, S.; Hirano, M.; Kamiya, T.; Hosono, H. Solid State Syntheses of $12\text{SrO}\cdot 7\text{Al}_2\text{O}_3$ and Formation of High Density Oxygen Radical Anions, O^- and O^{2-} . *Chem. Mater.* **2008**, *20*, 5987–5996. [[CrossRef](#)]
36. Lourenço, R.R.; Angélica, R.S.; Rodrigues, J.D.A. Preparation of refractory calcium aluminate cement using the sonochemical process. *Mater. Res.* **2013**, *16*, 731–739. [[CrossRef](#)]
37. Sango, H.; Miyakawa, T. Synthesis of $3\text{CaO}\cdot \text{Al}_2\text{O}_3\cdot 6\text{H}_2\text{O}$ in aqueous solution under the atmospheric pressure and rehydration of their thermal decomposition products. *Gypsum Lime* **1987**, *207*, 26–36.
38. Umar, A.; Hahn, Y.B. *Metal Oxide Nanostructures and Their Applications*; American Scientific Publishers: Santa Clarita, CA, USA, 2009.
39. Teleki, A.; Wengeler, R.; Wengeler, L.; Nirschl, H.; Pratsinis, S. Distinguishing between aggregates and agglomerates of flame-made TiO_2 by high-pressure dispersion. *Powder Technol.* **2008**, *181*, 292–300. [[CrossRef](#)]

